Electronic Supplementary Material (ESI) for Physical Chemistry Chemical Physics.

The Reaction Current Distribution in Battery Electrode Materials Revealed by XPS-Based State-of-Charge Mapping

Alexander J. Pearse[a], Eleanor Gillette[b], Sang Bok Lee[a], Gary W. Rubloff[a]

Supplementary Information

S1. First Principles Calculation of Expected XPS Spectra

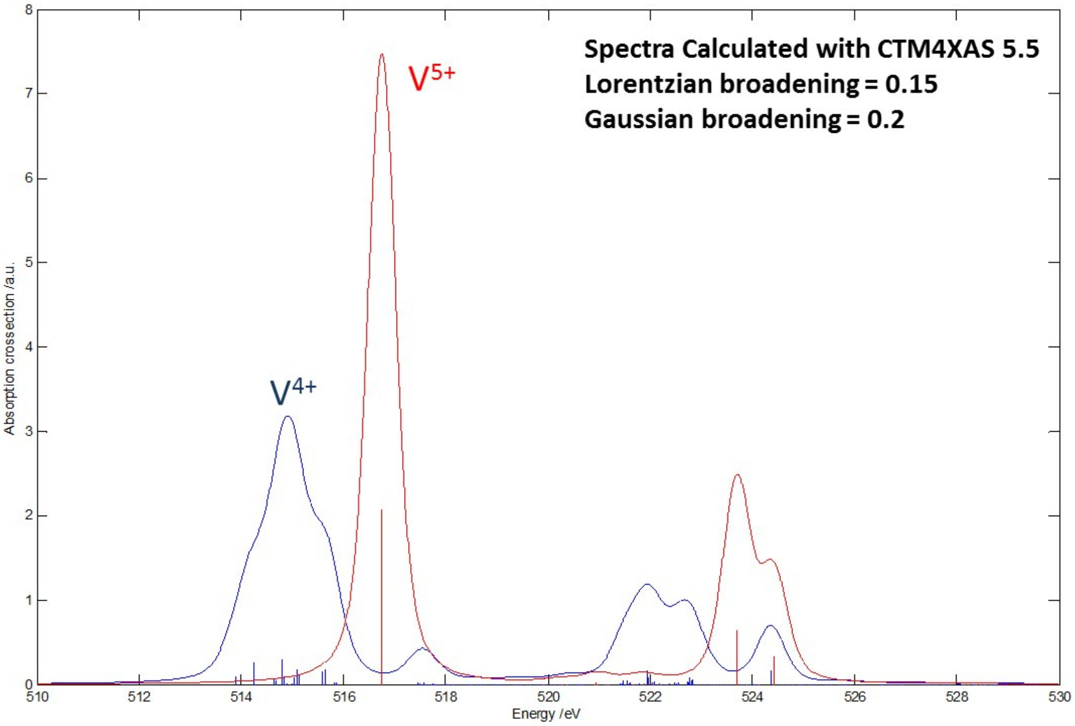

Figure S1: Calculated XPS spectra for V^{4+} and V^{5+} ions using CTM4XAS 5.5 and approximate broadening. This calculation illustrates the primary nonsymmetrical feature of the V^{4+} ion, which is the shoulder on the high binding energy side of the j=3/2 peak.

An accurate measurement of the SOC depends on a reliable deconvolution of the V 2p *j*=3/2 peak into contributions from V^{5+} and V^{4+}. While it is almost universal in the literature to assign a single peak to the V^{4+} state when fitting XPS data, we find that this is not a reliable fitting scheme when the area of the V^{4+} component is comparable to or exceeds that of the V^{5+} component. A closer examination of the physics behind the excitation of the V^{4+} ion reveals that this component is intrinsically a multiplet due to additional splitting in the final state. The electronic configuration of the V^{4+} ion is $[Ar]3d^1$, and thus possesses an unpaired electron in the valence band. This electron will then couple with the 2p core hole generated after photoexcitation, and result in additional exchange splitting in the final state. This effect, which occurs for most transition metal ions with net spin in the valence band, was explored by Gupta and Sen[1], who predicted a lineshape for V^{4+} which is asymmetric to the high binding energy side. A numerical simulation of the V^{4+} multiplet structrure using CTM4XAS 5.5[2] shows this feature. For our fitting, we use the simplest physically justified model for exchange splitting, which considers only the interaction between the core hole and the single 3d electron. This spin-spin interaction should produce two peaks with an intensity ratio[3] of $I_R = \frac{S+1}{S} = 3$ for $S = 1/2$. Our lineshape for V^{4+} thus contains two components of the same FWHM with a fixed area ratio of 3:1 and a fixed separation of 0.7eV, based on measurements[4] of single crystal LiV_2O_5, which results in accurate quantification as discussed below. While we exclude more detailed physics such as the crystal field or multi-body exchange effects in the fitting, which would likely decrease I_R, we note that the quantification of the V^{4+}/V^{5+} ratio is quite insensitive to $2 < I_R < 3$.

S2. Discharge Curve for V_2O_5

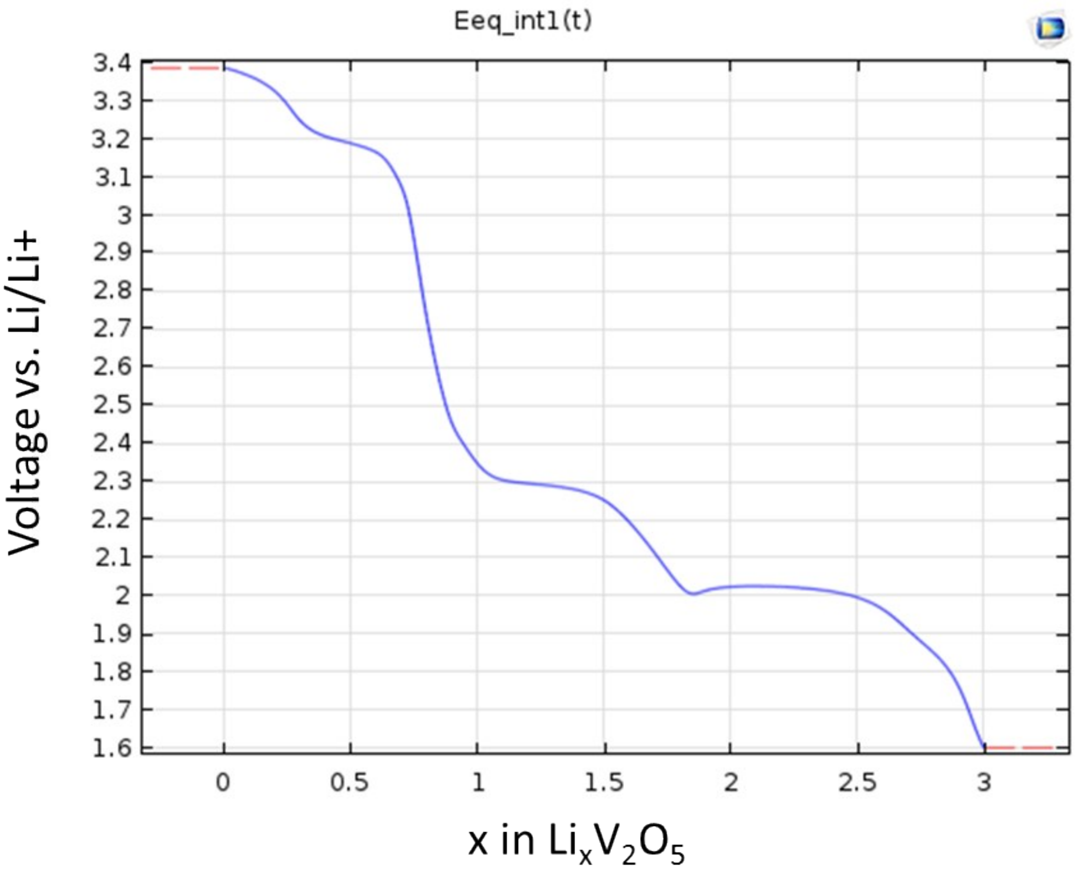

Figure S2: Equilibrium discharge curve for Li insertion into ALD V_2O_5. Data taken from a film grown on a planar Au current collector discharged at a C/10 rate. This curve is parameterized and used in the COMSOL simulations.

S3. High-resolution Chemical State Map of A Test Electrode

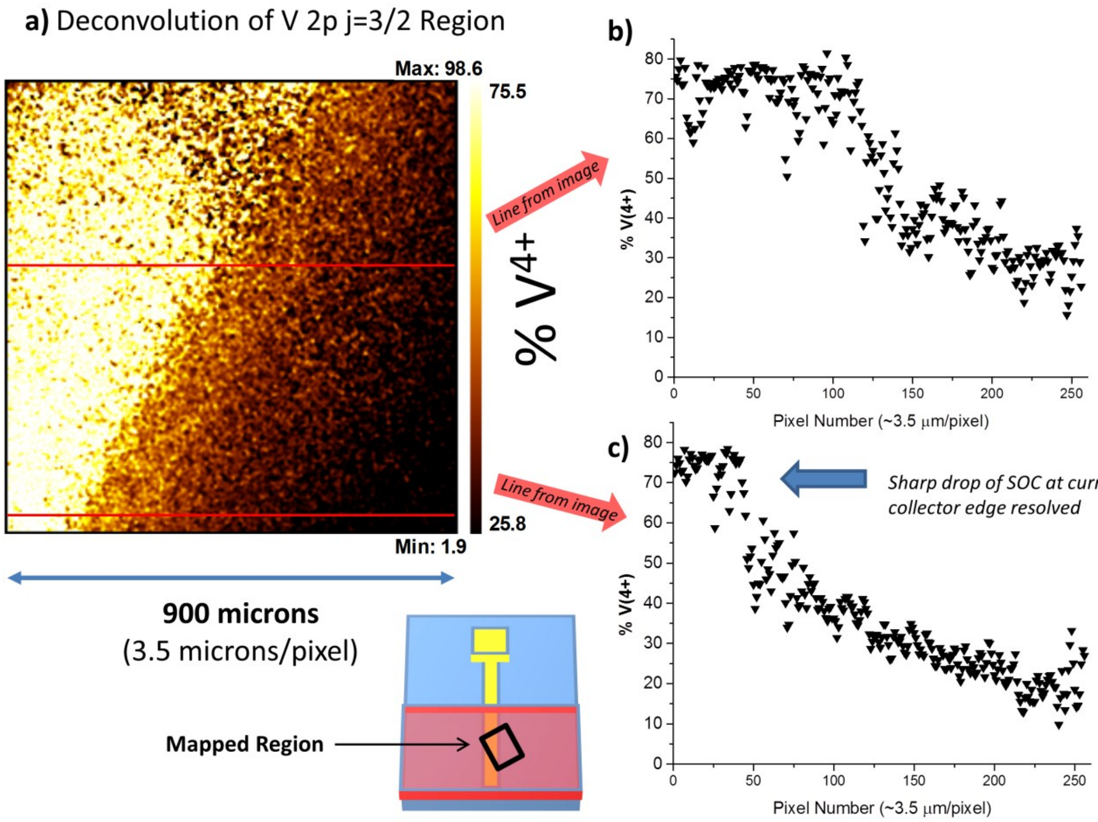

Figure S3: An example of the high resolution chemical state mapping capability of modern XPS instrumentation. The map in (a) is derived from a direct photoelectron image of a portion of the test electrode shown in the schematic below the image. Each pixel represents a spectrum of the V 2p j=3/2 region in a third dimension (energy). Each pixel is then subjected to deconvolution into V^{5+} and V^{4+} components through principle component analysis of the whole image using CasaXPS. (b) and (c) show lines from the image demonstrating the SOC profile away from the current collector. This method achieves a spatial resolution for differentiating valence state of approximately 20-30 microns and could likely be improved further.

S4. Details of COMSOL Model

Below is a table of the parameters and variables used in the numerical model as implemented in COMSOL.

Model Parameter	Description	Value/Units
σ_s	Initial electronic conductivity of V_2O_5	4 mS/cm
D_s	Lithium diffusion constant in V_2O_5	10^{-11} cm^2/s [5]
i_{ex}	Exchange current density of Li insertion in V_2O_5	0.0016 mA/cm^2 [6]
D_{el}	Diffusion constant of Li in propylene carbonate	$5.5 \times 10^{-6}\, cm^2/s$
κ	Electrolyte conductivity	6 mS/cm [7]
t_+	Li transport number	0.28 [8]
l	Width of current collector	0.05 cm
R	Gas constant	8.314 J/(K mol)
T	Temperature	293.15 K
F	Faraday's constant	96485 C/mol
c_l	Li ion concentration in electrolyte	Mol/m^3
c_s	Li ion concentration in electrode	Mol/m^3

The geometry represented is a 2D cross section of the active region of the test electrodes (shown below, not to scale). The physical thickness of the gold strip is neglected for simplicity in this model, and instead current is applied in a defined region at the bottom of the V2O5 region. The electrolyte region is meshed with a free triangular mesh, and the electrode region is meshed with a custom rectangular mesh, which increases in density near the edges of the current collector.

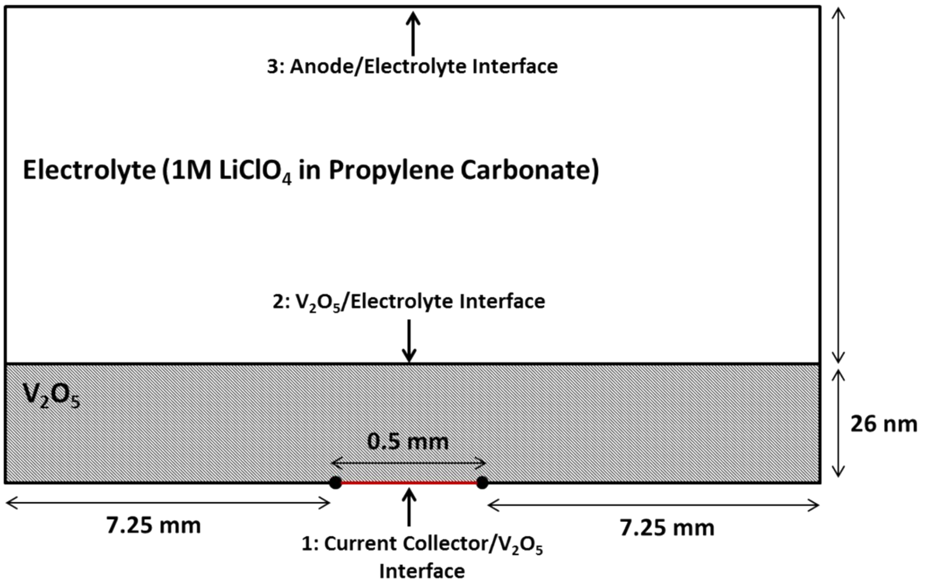

Figure S4: Schematic of the COMSOL model's geometry. Not to scale.

The governing equations can be separated into the bulk transport physics in the electrolyte and V2O5 regions, and the coupling equations enforced at interfaces 1 (the current collector/V_2O_5 boundary), 2 (the electrode/electrolyte interface) and 3 (the electrolye/anode interface). Mechanically speaking, these equations are implemented using the Lithium-Ion Battery and Transport of Dilute Species modules of COMSOL Multiphysics 5.1, along with a few custom conditions and added material data. We note that in COMSOL, the normal vector n (as used below) is conventionally positive in the "outward" direction of each domain.

Electrolyte Domain:

Transport in the electrolyte is described by concentrated solution theory.[9] One equation (S1) defines the current vector i_L and local reaction current density j_{Li}, a second (S2) describes the number flux of Li ions N_L, and a third (S3) describes ion conservation:

$$j_{Li} = \nabla \cdot i_L = \nabla \cdot \left[-\kappa \nabla \varphi_l + \frac{2\kappa RT}{F}(1 - t_+)\left(1 + \frac{\partial \ln f}{\partial \ln c_l}\right)\nabla \ln c_l \right] \tag{S1}$$

$$N_L = -D_l \nabla c_l + \frac{i_L t_+}{F} \tag{S2}$$

$$\frac{\partial c_l}{\partial t} + \nabla \cdot N_L = 0 \tag{S3}$$

In the bulk of the electrolyte, $j_{Li} = 0$. In addition, we neglect the activity dependence term in equation S1 due to low overall concentration variations under the simulated conditions, i.e. $\frac{\partial \ln f}{\partial \ln c_l} = 0$. The initial conditions are set to $c_l = 1M$ uniformly.

Electrode (V_2O_5) Domain:

Electrical transport in the electrode region is described by Ohm's law, and the transport of intercalated Li ions is described through Fick's laws for dilute species diffusion. In the bulk, this simply describes ion conservation.

$$-\sigma_s(c)\nabla\varphi_s = i_s \tag{S4}$$

$$\frac{\partial c_s}{\partial t} + \nabla\cdot\left(-D_s\nabla c_s\right) = 0 \tag{S5}$$

Interface 1: Current Collector/V$_2$O$_5$ Coupling

At the interface of the gold strip and the V$_2$O$_5$, the total current passing through the cell is set by the following boundary condition:

$$\int_{-l/2}^{l/2} i_s\cdot n\,dl = -\,l\cdot I_{app} \tag{S6}$$

This allows us to set a fixed average current density but allow the normal current density to vary across the length of the boundary, which leads to more realistic results than forcing a uniform current density. The value I_{app} is found from the total current applied to the chip divided by the total area of the current collector buried under the electrode. A no-flux condition for Li ions is also enforced here.

Interface 2: Electrolyte/V$_2$O$_5$ Coupling

At the electrolyte/V$_2$O$_5$ interface, the reaction current j_{Li} is controlled through Butler-Volmer kinetics. This reaction removes Li ions from the electrolyte and adds an equal flux of Li ions into the electrode, controlled by the local difference in electric potential $\varphi_S - \varphi_L$. The equilibrium potential $U(c_s)$ of the insertion reaction changes as a function of the surface concentration of lithium ions and is taken from the curve shown in Figure S2. We assume a constant exchange current density i_{ex}, as testing showed variations in i_{ex} had a relatively small effect on the RCD but introduced some instability into the model.

$$j_{Li} = i_{ex}\left[e^{\frac{\alpha_a F(\varphi_S - \varphi_L - U)}{RT}} - e^{\frac{-\alpha_c F(\varphi_S - \varphi_L - U)}{RT}}\right] \tag{S7}$$

$$n\cdot i_s = j_{Li} \tag{S8}$$

$$n\cdot i_L = -\,j_{Li} \tag{S9}$$

$$n\cdot N_L = -\frac{j_{Li}}{F}\left(1 - t_+\right) \tag{S10}$$

Interface 3: Electrolyte/Anode Coupling

The electrolyte/anode interface is modeled as an ideal lithium anode using Butler-Volmer kinetics in the same form as Equations S7-S10, with the additional boundary condition that $\varphi_{S,Li} = 0$. This fixes the potential of the V_2O_5 electrode to be referenced to Li/Li+.

S5. Simulated Discharge Curves for Different Values of Gamma

Figure S5: Simulated discharge profiles for the test electrode geometry under different assumptions of peak conductivity. (a) shows simulated discharge profiles for a model with no change in the electronic conductivity. These potentials are references to the fixed potential (V=0) of the ideal lithium anode. They do not include double layer capacity, which would otherwise lead to a slight downward slope at the beginning of discharge.

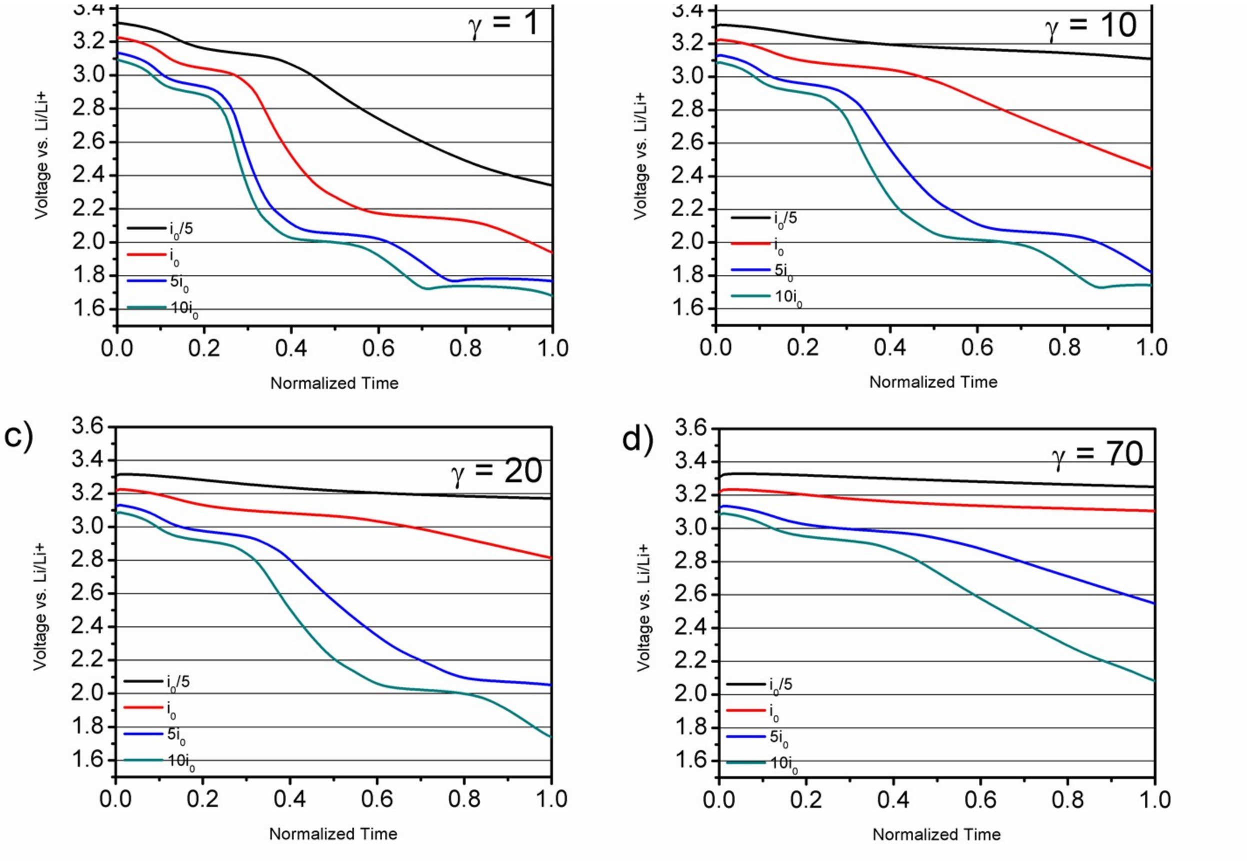

S6. Experimental Details

1. Chip Construction

Battery test chips were constructed using quartz wafers as an inert support. A 5nm ALD Al_2O_3 film was first deposited as a nucleation promoter for the subsequent V_2O_5 ALD process using a Beneq TFS 500 ALD reactor at 150C. Patterned electrodes were fabricated via thermal evaporation of 5nm Cr/ 45nm Au through a laser cut stainless steel evaporation mask. The wafer was then diced from the back side into individual chips of dimensions 15x25 mm, and crystalline V_2O_5 was deposited using a previously described ozone/VTOP ALD process in a Beneq TFS 500 reactor at 170C.[10] The ALD film was patterned via physical masking by clamping a precut piece of silicon to the top half of the chip using a metal clip, defining a 10x15 mm or 10x10 mm exposed area. Residual V_2O_5 on the edges of the chip was scraped off with a diamond pen to ensure no electrical connection to any material deposited on the back side of the device. ALD Film thickness was confirmed using optical ellipsometry.

2. Electrochemical Testing

Three-electrode electrochemical testing was performed in a beaker cell inside an Ar-filled glovebox (H_2O and O_2 <1ppm) using a Biologic VSP. In all cases, the electrolyte used was 1M $LiClO_4$ in anhydrous propylene carbonate (typically 25mL) with separate metallic Li counter and reference electrodes. Each chip was secured with copper tape, which also acted at the electrical contact, on the inside of a glass beaker. All areas of the chip not covered with the V_2O_5 film were encapsulated with parafilm to prevent contact between uncoated sections of the gold current collector and the electrolyte. Generally, the beaker was filled to a depth so that the active region of the chip was completely immersed in the electrolyte. All currents applied to the chip were normalized to the area of V_2O_5. After discharge or charge, the chips were immediately (within a maximum of 60 seconds) removed from the electrolyte and briefly rinsed with ethanol to remove the low vapor pressure solvent and residual salts and loaded into the XPS.

3. XPS

After electrochemical alteration, the chips were loaded into the XPS for characterization. Measurements were taken with a Kratos AXIS Ultra DLD instrument using monochromated Al Kα x-rays as the excitation source (operated at 144W). The instrument was operated in hybrid (magnetic immersion) mode using the slot aperture for general scans, or the 110µm or 55µm aperatures for line scans. Survey spectra were taken with a step size of 1 eV and a pass energy of 160 eV. High resolution spectra were collected using pass energy 20 eV and a 0.1 or 0.05 eV step size. Due to the chip construction, the V2O5 films were electronically floated (isolated from the instrument ground) and charge compensation was provided entirely with the Kratos charge neutralization system. In order to perfom line scans, each chip was assigned a coordinate system relative to the manipulator arm coordinate system, which was found by measuring the positions of the corners of the chip. For each chip, the alignment of the analyzer and the sample alignment camera was checked by mapping the location of an uncoated Au feature. Line scans were taken at the approximate midpoint along the length of the current collector. Peak fitting was performed using CasaXPS, using 50/50 products of Gaussian/Lorentzian lineshapes (GL(50) within CasaXPS) on a Shirley background and a least-squares fitting algorithm. Quantification was performed using peak area corrected for the photoionization cross section of each element and the instrument geometry. Inelastic mean free path lengths were calculated with the QUASES-IMFP-TPP2M software.

4. COMSOL

COMSOL simulations were performed using COMSOL Multiphysics version 5.1. Simulations used a time-dependent solver with a relative tolerance of 0.0001 using the Backwards Differentiation Formula option. The Transport of Dilute Species and Lithium-Ion Battery modules were used in implementing the physics.

S7. SEI Formation on V_2O_5

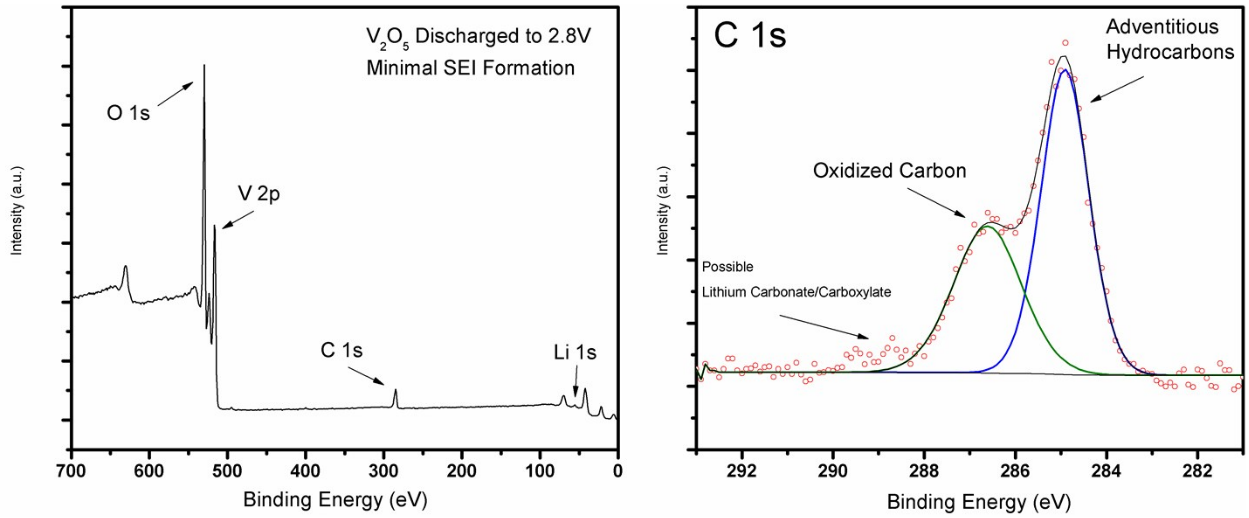

Figure S6: XPS data showing minimal SEI formation on V2O5 discharged to 2.8V vs. Li/Li+. (Left) A survey spectrum showing a small C 1s peak as the only non-expected element. (Right) High-resolution data showing adventitious hydrocarbon, as well as an oxidized carbon species associated with the SEI. A small signal possibly associated with inorganic lithium carbonates can be seen at approx. 289 eV.

Supplementary References

1 R. Gupta and S. Sen, *Phys. Rev. B*, 1975, **12**.

2 E. Stavitski and F. M. F. de Groot, *Micron*, 2010, **41**, 687–694.

3 G. Garreau, V. Schorsch, E. Beaurepaire, J. Parlebas, O. Speder and P. Rennert, *J. Phys. IV*, 1994, 3–7.

4 M. J. Konstantinović, S. Van den Berghe, M. Isobe and Y. Ueda, *Phys. Rev. B*, 2005, **72**, 125124.

5 Z. Lu, M. D. Levi, G. Salitra, Y. Gofer, E. Levi and D. Aurbach, *J. Electroanal. Chem.*, 2000, **491**, 211–221.

6 C. A. C. Sequeira and D. M. F. Santos, *ECS Trans.*, 2010, **25**, 121–132.

7 B. Klassen, R. Aroca, M. Nazri and G. a. Nazri, *J. Phys. Chem. B*, 1998, **102**, 4795–4801.

8 K. M. Abraham, in *Applications of Electroactive Polymers*, p. 94.

9 T. F. Fuller, M. Doyle and J. Newman, *J. Electrochem. Soc.*, 1994, **141**, 1–10.

10 X. Chen, E. Pomerantseva, K. Gregorczyk, R. Ghodssi and G. Rubloff, *RSC Adv.*, 2013, **3**, 4294.